

Design, experimental investigation and multi-objective optimization of a small-scale radial compressor for heat pump applications

J. Schiffmann^{a,*}, D. Favrat^b

^a Fischer Engineering Solutions AG, Birkenweg 3, CH-3360 Herzogenbuchsee, Switzerland

^b Ecole Polytechnique Fédérale de Lausanne, EPFL STI IGM LENI, Station 9, CH-1015 Lausanne, Switzerland

ARTICLE INFO

Article history:

Received 24 May 2009

Received in revised form

24 September 2009

Accepted 8 October 2009

Available online 4 November 2009

Keywords:

Domestic heat pump

Oilfree compressor

Centrifugal compressor

Design optimization

ABSTRACT

The main driver for small scale turbomachinery in domestic heat pumps is the potential for reaching higher efficiencies than volumetric compressors currently used and the potential for making the compressor oil-free, bearing a considerable advantage in the design of advanced multi-stage heat pump cycles. An appropriate turbocompressor for driving domestic heat pumps with a high temperature lift requires the ability to operate on a wide range of pressure ratios and mass flows, confronting the designer with the necessity of a compromise between range and efficiency. The present publication shows a possible way to deal with that difficulty, by coupling an appropriate modeling tool to a multi-objective optimizer. The optimizer manages to fit the compressor design into the possible specifications field while keeping the high efficiency on a wide operational range. The 1D-tool used for the compressor stage modeling has been validated by experimentally testing an initial impeller design. The excellent experimental results, the agreement with the model and the linking of the model to a multi-objective optimizer will allow to design radial compressor stages managing to fit the wide operational range of domestic heat pumps while keeping the high efficiency level.

© 2009 Elsevier Ltd. All rights reserved.

1. Introduction

According to the International Energy Agency [1] the worldwide energy fraction consumed by the residential sector accounts for 35% of the total energy consumption, out of which 75% are used for space and tap water heating. As domestic heating requires relatively low temperature levels (30 °C for floor space heating and 60 °C for tap water), renewable energy sources (environmental heat) may offer an interesting alternative to fossil fuels. Recently Favrat et al. [2], have introduced an exergy efficiency indicator, compared different heating technologies and reported on the significant advantage of heat pumps in this respect. Other studies also show that the future combination of efficient trigeneration techniques with advanced hybrid fuel cell–gas turbine systems and heat pumps could further improve the prospects for a more rational use of energy (Burer et al. [3]).

The targeted topic in this particular study is the design optimization of a radial compressor for driving a heat pump for domestic heating applications. The main driver for small scale turbomachinery in low power heat pumps is the potential for

reaching higher efficiencies than volumetric compressors currently used in these machines and the potential for making the compressor oil-free, which bears a considerable advantage in the design of advanced multi-stage heat pump cycles. In an earlier paper Schiffmann et al. [4] investigate on the feasibility of a twin-stage radial flow compressor for driving a two stage heat pump. They come to the conclusion that a compressor unit with two impellers of 20 and 18 mm tip diameter, rotating at 250 krpm is technically feasible. Recently Schiffmann and Favrat [5] have published experimental data demonstrating the technical feasibility of a small scale, oil-free and direct driven turbocompressor for domestic heat pump applications. Their proof of concept consisted of an oil-free gas bearing supported radial turbocompressor with a tip diameter of 20 mm that was tested to speeds up to 210 krpm, reaching pressure ratios in excess of 3.3 and internal isentropic compressor efficiencies of up to 79%.

Centrifugal compressors are extensively used in a wide spectrum of industrial applications, with nearly any combination of pressures, powers, applications and gases. Turbochargers for internal combustion engines alone embrace automotive as well as marine applications, with impeller diameters varying from approximately 30 mm to more than 1 m. Other typical applications are micro-turbine generators, industrial refrigeration cycles and helicopter gas turbines where pressure ratios of up to 1:10 are

* Corresponding author. Tel.: +41 (0)62 956 88 50; fax: +41 (0)62 956 22 00.
E-mail address: juerg.schiffmann@fischerprecise.ch (J. Schiffmann).

Nomenclature*Roman symbols*

\dot{m}	mass flow [kg s^{-1}]
Re	Reynolds number
A	section [m^2]
b	channel width [m]
c	absolute velocity [ms^{-1}]
C_f	friction coefficient [–]
d	diameter [m]
D_f	diffusion coefficient [–]
D_h	Hydraulic diameter [m]
e_{back}	impeller backplate clearance [m]
e_{blade}	impeller blade thickness [m]
E_{el}	electric energy [J]
e_{is}	specific isentropic work [J kg^{-1}]
e_{tip}	impeller tip clearance [m]
h	specific enthalpy [J kg^{-1}]
K_f	disc friction coefficient [–]
K_L	pressure loss coefficient [–]
l	axial length [m]
L_h	hydraulic length [m]
N_{Bl}	number of main blades [–]
n_d	number of days [–]
N_{rot}	rotational speed [rpm]
N_{Sp}	number of splitter blades [–]
p	pressure [Pa]
r	impeller radius [m]
Ra	surface roughness [m]
T	temperature [$^{\circ}\text{C}$]
u_t	tip velocity [ms^{-1}]
w	relative velocity [ms^{-1}]

Greek symbols

α	absolute flow angle [deg]
β	relative flow angle [deg]

η	efficiency [–]
η_{is-k}	isentropic compressor efficiency [–]
η_{y-k}	seasonal isentropic compressor efficiency [–]
μ	viscosity [Pa s]
Π	pressure ratio [–]
ρ	density [kg m^{-3}]

Subscripts

1	inducer inlet
2	impeller inlet
3	impeller inlet throat
4	impeller discharge
5	diffuser discharge
7	volute discharge
θ	tangential component
air	Air
bl	blade loading & diffusion
cl	clearance
df	disc friction
ext	external
h	hub
in	inlet condition
inc	incidence
ind	inducer
is	isentropic
m	Meridional component
meas	measured value
opt	optimum
out	exhaust condition
rc	recirculation
rms	rms-value
s	shroud
sf	skin friction
St1	stage 1
St2	stage 2
tt	total–total
water	water

required, ideally on a single compressor stage. In aerospace applications saving weight is the main driver, leading to a run for highest possible pressure ratios on one stage. Recently the experimental investigation of a single stage 1 MW impeller with a pressure ratio 1:11 processing air was presented by Higashimori et al. [6]. The diversity in terms of applications, pressure ratios and powers is further increased by different operational requirements. In some stationary industrial applications the aim of the compressor is to deliver a nominal mass flow and pressure ratio with the least possible energy consumption, whereas in other applications the emphasis is rather on a wide range of possible pressure ratios and mass flows, necessarily leading to a compromise on efficiency. The present publication proposes a way to facilitate the design of small scale turbocompressors requiring operation on a wide range in terms of pressure ratio and mass flows.

The focus on the design procedures, performance prediction and especially on the efficiency gain of radial compressors is still today mainly driven by large industrial compressor stages. Today's small scale turbomachinery applications, however, are essentially driven by micro-gas turbine applications. Already in 1980 Strong [7] presented a directly fired heat pump, where an Organic Rankine Cycle turbine drove the compressor of a reversed Organic Rankine heat pump cycle. The radial compressor was 26.2 mm in diameter and rotated at 160 krpm. The measured efficiency was 60% at a pressure ratio of 6.65 and a mass flow of 0.027 kg s^{-1} . In 1996 Yun and Smith

[8] presented a study of a two stage compressor for automotive air-conditioners. The fluid was an R123 and the impeller diameters 48 and 38 mm delivering pressure ratios of 3.2 and 1.94. The pressure ratios were unbalanced in order to achieve the best possible efficiency, taking into account the tip clearance losses. The overall peak efficiency including the intercooler between the two stages was predicted to be around 77%. In 1998 Mehra et al. [9] presented a theoretical study on a small gas turbine motor with an electrical output power of 10–40 W contained in a volume smaller than 1 cm^3 . Due to size and manufacturing issues the proposed impellers were composed of 2D vanes. Calculations based on CFD predicted a pressure ratio of 4.4 and an efficiency of 63%. Two years later Frechette et al. [10] showed first results of the turbine of the small 2D turbine reaching 1.4 Mrpm and an output of 5 W. However, neither efficiencies nor turbine maps are published. In 2004 Epstein [11] presents the state of the art of the MIT micro-gas turbine project as a whole, giving, among other, insights in the manufacturing based on semiconductor industry derived processes allowing to etch silicon and silicon carbides to submicron tolerances. In 2001 Isomura et al. [12] present the feasibility study of a slightly larger gas turbine generator with a power output of 100 W, using 3D radial impellers with a compressor pressure ratio of 3, a rotational speed of 870 krpm and a predicted efficiency of 65%. The drivers for the micro-turbine generators are mainly military applications; the power density of these machines is

considerably larger than today's batteries, leading to lighter power supply with an extended autonomy. In 2003 Johnston et al. [13] published measured data on a 12 mm radial compressor (also for gas turbine generators). The tests were performed at speeds up to 420 krpm (50% of the design speed), reaching pressure ratios of 1.6 and efficiencies in excess of 70%. The impeller made of silicon-nitride was manufactured using a near net shape molding process presented by Kang et al. [14]. In 2006 Isomura et al. [15] demonstrated the feasibility of the small size compressor rotating at 720 krpm reaching a pressure ratio slightly higher than 2 at a measured isentropic efficiency in excess of 60%, using a 3D impeller wheel machined on a 5-axis milling machine.

According to the above mentioned studies small turbomachinery can achieve a reasonable efficiency level, but are less efficient than larger impellers. The investigation therefore targets the identification of the loss mechanisms that impellers suffer from when their size decreases and what the measures could be to minimize or even prevent size specific losses. Both Johnston [13] and Sirakov [16] have identified the main issues related to small size turbomachinery:

Low Reynolds number and surface roughness are two very important limiting issues for reaching good efficiencies. Casey [17] has measured a drop of 10 points in stage efficiency between impellers operated at high (7×10^4 – 1.2×10^5) and at low Reynolds numbers (2×10^4). Further he has shown that the skin friction in the impeller channels can be modeled by an equivalent pipe flow. The friction coefficient of a turbulent pipe flow is a function of the Reynolds number and of the relative surface roughness (Moody [18]). On the Moody-diagram it becomes clear, that the relative surface roughness has a large impact on the friction coefficient: the rougher the surface compared to the overall hydraulic diameter the higher the skin friction losses. Assuming a given absolute surface roughness resulting from a machining operation like milling or casting, then the relative surface roughness increases with decreasing size of impeller. The consequence is that the skin friction losses increase with decreasing impeller size for a given Reynolds Number. The skin friction, however, can be decreased if manufacturing procedures that allow a better surface finish are applied. According to the operation points shown in Table 1 an impeller with a diameter of 20 mm and an exit blade width of 1 mm processing R134a would operate at a Reynolds number between 1.8×10^5 and 2.5×10^5 . Therefore in this particular application the low impeller size is not expected to have a penalty effect on the efficiency due the Reynolds numbers.

The Tip clearance is the second limiting factor. It has been shown in several publications [19–23], that the efficiency of radial impellers is seriously impaired by large relative tip clearances. In general it can be stated that an increase of 10% of the relative tip clearance (e_{tip}/b_4 , see Fig. 2) reduces the efficiency by 3–4 points. As the impellers are getting smaller in size it becomes more and more difficult to keep the relative tip clearance small due to

manufacturing tolerances on one hand and due to the bearing technology on the other. If a large impeller had a discharge blade width of 100 mm and a tip clearance of 1 mm then a small compressor stage with a discharge width of 1 mm would require a tip clearance of 10 μm for reaching the same relative clearance losses. Such a tip clearance is, however, difficult to reach in terms of assembly and manufacturing tolerances. The hydrostatic oil bearings, as currently used in automotive turbochargers, present overall clearances in the order of 0.1–0.3 mm, and are therefore responsible for additional clearance losses as a touchdown of the impeller on the shroud surface must be avoided. In this particular application and in small turbomachinery in general the design of the system needs to allow to minimize the tip clearance. It follows that the choice of the bearing technology as well as the assembly tolerances, directly affect the efficiency of the impeller.

Minimum feature size. When manufacturing processes such as milling and molding are involved, there is a size where the geometry cannot be scaled down deliberately, the blade geometry proportions cannot be kept similar to the ones in large impellers: in the impeller presented below the blade thickness was chosen to be 0.2 mm which corresponds to 20% of the exit channel width (b_4). In larger impellers this latter value is rather around 5–10%. The leading edges cannot be as sharp as in large impellers. The wider blades may reduce tip leakage, but the blunt leading edge will lead to higher blockage in the inducer region and finally at the impeller discharge. Blockage reduces the effective flow passage on one hand, which can be taken into account by increasing the channel section. On the other hand, blockage leads to a flow distortion at the impeller discharge. Increased flow distortion at the diffuser inlet will lead to decreased pressure recovery coefficients and therefore to lower stage efficiency. To the authors knowledge there is today no tool available to model the added losses due to the minimum feature size in small impellers.

Non-adiabatic effect The heat generated in the compressor wheel is proportional to v_4^3 (volume) and the heat transfer proportional to r_4^2 (surface). When the impeller size decreases the ratio between the available surface and the volume increases. This may lead to situations where the flow process in the impeller cannot be treated as purely adiabatic anymore [16]. Gong et al. [24], Epstein [11] and Isomura et al. [12] have investigated the influence of heat addition in small turbomachinery with shroud wall temperatures up to 1000 K, leading to additional losses in the order of 20–40 points. Therefore in applications where high exhaust gas temperatures may be reached or where hot sources are very close (micro-turbine generators), the non-adiabatic effect may depreciate the overall efficiency considerably, and thermal insulation between the compressor discharge and inlet becomes crucial. In the application of the heat pump compressor, however, this effect is likely not to affect efficiency. The hydrocarbon based refrigerants have in general very low adiabatic coefficients (κ), and therefore the temperature difference between inlet and exhaust is considerably lower than for compressors processing air. The temperature of the processed gas around the compressor will lie in the range between 258 and 303 K (first stage).

As a summary out of Reynolds number, tip clearance, minimum feature effects and non-adiabatic issues only the relative surface roughness, the tip clearance and the minimum feature size are topics that need closer attention for this particular refrigerant compressor. As explained earlier the tip clearance issue can be taken care of by choosing the most suitable bearing technology. Little experience has been made on the impact of the minimum feature effects and little can be done to minimize these if conventional machining is used for the impeller manufacturing. The surface roughness is limited by the machining process (milling), but in a later process it can be improved by a polishing process.

Table 1

A summary of the requirements for some typical operational points for the 1st and the 2nd stage of the heat pump compressor processing R134a refrigerant, for an air-water heat pump delivering a heat rate of 12 kW at 60 °C for an external air temperature of –12 °C.

OP	1	2	3	4	5
T_{air} [°C]	–12	–7	2	7	12
T_{water} [°C]	60	55	50	45	40
p_{in} [MPa]	0.144	0.177	0.251	0.302	0.36
Π_{St1} [–]	4.2	3.3	2.4	2	1.7
\dot{m}_{St1} [kg s ^{–1}]	0.053	0.043	0.024	0.016	0.005
Π_{St2} [–]	2.8	2.6	2.2	1.9	1.7
\dot{m}_{St2} [kg s ^{–1}]	0.08	0.061	0.032	0.015	0.006

The specifications related to the compressor requirements for the targeted domestic heat pump application have been calculated using heat pump modeling tools that have been developed by Zehnder [25]. A typical one family house situated in middle Europe with a hydraulic radiator system requires a heat rate of 12 kW delivered at 60 °C for an external air temperature of –12 °C, with the required heat rate decreasing linearly with increasing external air temperature. At temperatures of 15 °C no heating is required anymore [26]. The operational range of the heat pump has been split into 5 typical points corresponding to air temperatures of –12, –7, 2, 7 and 12 °C. For each of these external air temperatures the corresponding hot water temperatures are specified through the SIA norms [27]. The specification for the two compressor stages are summarized in Table 1, based on the use of R134a as a refrigerant. A detailed analysis on the choice of the refrigerant fluid is given by Schiffmann [28,5]. The application of a centrifugal compressor for driving a domestic heat pump clearly demands a wide range of pressure ratios and of mass flows (see Table 1). The requirement in terms of efficiency can be stated as the minimization of the energy consumption over a whole heating season. This does not necessarily mean a maximum efficiency on the complete range but rather an efficiency distribution such that the yearly energy consumption of the heat pump system is minimized. Therefore operational points that do not occur often during the heating season do not have an impact as high as frequent ones. In order to efficiently design an optimum impeller geometry for best matching the operational range of a continuously running heat pump compressor, a general, robust and rapid design tool is required.

2. The initial design

The feasibility study by Schiffmann et al. [4] has shown that the development of radial turbocompressor for heat pumps bears considerable technological risks. It was therefore decided to build a single stage compressor serving as proof of concept before stepping further on. One of the design-criteria was that the single stage compressor should be able to fit the specifications of the 1st stage of a twin-stage heat pump (see Table 1).

A first design of the impeller for the first stage compressor has been performed by Schiffmann and Favrat [29] using a commercial design package. As a limitation in terms of size, the minimum impeller diameter was set to 20 mm in order to keep the impeller machinable on an available conventional five-axis milling machine.

The main geometrical dimensions of the impeller resulting from the initial design procedure are listed in Table 2. In order to manage the wide mass-flow range required by the heat pump it was necessary to use a vaneless diffuser instead of a more efficient channel or even airfoil diffuser. In order to decrease the degree of complexity it was decided to avoid the use of inlet guide vanes. Using the available 1D, 2D and subsequently the 3D tool the impeller geometry was improved in terms of fitting the specifications and improving the efficiency. In order to do so particular attention was given to the relative Mach number distribution along

the blade channels and to the suppression of secondary flows. The secondary flows are known to move the low momentum fluid of the boundary layers toward regions where the static pressure is low. They are responsible for the jet-wake mechanism resulting in an exit flow non-uniformity known to deteriorate the stage efficiency and reduce the stable operating range of the vaneless diffuser [30]. Zangeneh et al. [31] relate the generation of the secondary flows to the relative Mach number gradients: secondary flow generation occurs whenever there is a gradient of relative Mach numbers in the direction of vorticity in the flow field. Very little secondary flows are therefore generated in the inducer region due to the low boundary layer thickness. The region of high impact is the suction surface in the range of 30–80% of the blade channel length due to the high boundary layer thickness compared to the one on the pressure surface and in the inducer region. In order to avoid secondary flow generation in this region Zangeneh et al. [32], propose to reduce the relative Mach number gradients between the hub and the shroud on the suction surface. This mechanism has been applied for the detailed blade geometry design of this particular impeller [29].

Fig. 1 represents the speed range for the operational points 1, 2, 3 and 5 and the predicted internal isentropic efficiencies (total-total) as a function of the required pressure ratios and mass flows resulting from the prediction based on 3D-CFD calculations. At the maximum pressure ratio the mass flow is slightly inferior compared to the specified one. This is due to a compromise between maximizing the mass flow at high pressure ratios and reaching the specifications for the most common operation point [3]. The resulting compressor unit allows a continuous operation whenever the air temperature at the inlet of the evaporator is below 2 °C (Operation Points 1, 2 and 3). For external air temperatures above 2 °C an intermittent compressor operation mode will be necessary, as too much mass flow and therefore too much heating power is delivered. The CFD calculations predict a maximum internal isentropic efficiency in excess of 84%. The Finite Element Method has been used for mechanical stress calculations and for the prediction of the blade critical frequencies [29]. The low tip speed (262 m/s) compared to compressors operating with lighter gases than refrigerant, lead to relatively low mechanical stresses enabling the use of an easy to machine, conventional aluminum-alloy.

Although the available software package allows to efficiently design the compressor stage for a given nominal operation point, it does not allow an efficient and flexible optimization over a complete operational range as required by this particular application. In order to allow the overall optimization of the direct driven turbocompressor it was decided to generate an inhouse, one-dimensional compressor model that would allow a straightforward optimization and most of all lead to a flexible automatic design procedure including the optimization of the compressor on the complete operational range. Such an inhouse model will further easily allow to calibrate and adapt the different loss models.

3. Inhouse model

The flow in radial compressors is highly 3-dimensional and therefore difficult to model. Advanced design tools use 3D-CFD, which is time consuming and does not easily allow a large number of iterations for automatic optimization routines. An effective procedure to decrease the geometry optimization time is performed by teaching a neural network through CFD calculations. The neural network is then coupled to an Evolutionary Algorithm performing the geometry optimization. This procedure has successfully been applied by Demeulenaere and Hirsch [33] for optimizing

Table 2

A summary of the geometrical dimensions of the compressor stage designed with commercial software package. See Fig. 2 for nomenclature.

Inlet shroud radius	r_{2s}	[m]	0.0056
Tip radius	r_4	[m]	0.01
Tip width	b_4	[m]	0.0012
Diffuser exit radius	r_5	[m]	0.0165
Exit blade angle	β_4	[°]	–45

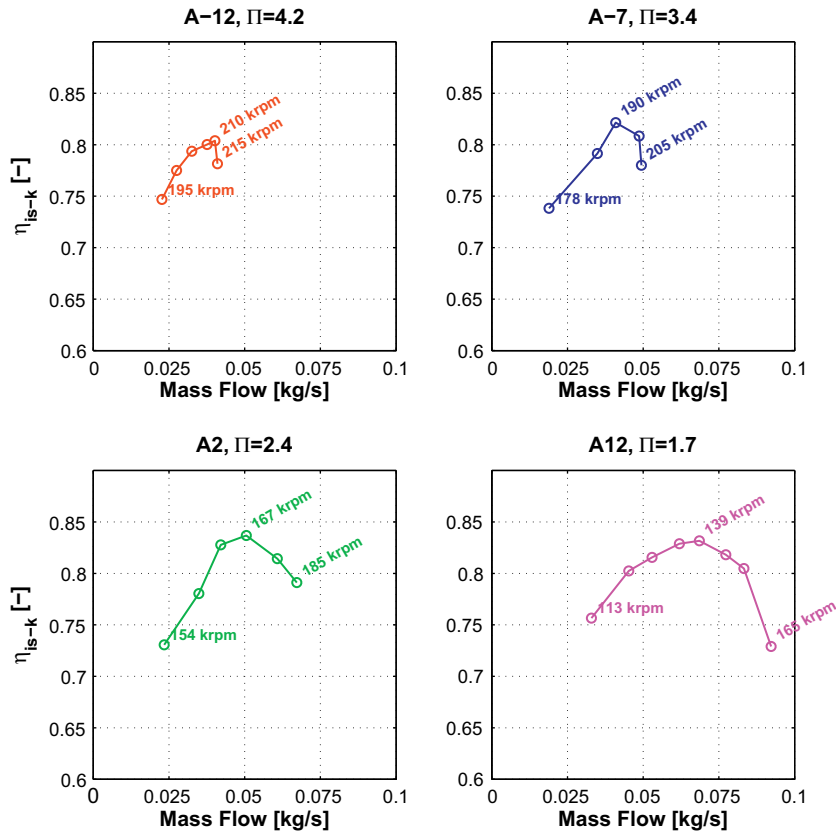


Fig. 1. The rotational speed range and the internal isentropic efficiencies as a function of the required pressure ratio and mass flow (final geometry), resulting from 3D-CFD calculations.

an axial turbine and by Harinck et al. [34] in the case of a radial turbine. The procedure is appropriate for modeling the impeller passage and the detailed blade shapes starting from an initial design and is therefore too complex and time consuming for defining a basic impeller layout.

Basic design tools are based on the velocity triangles and passage sections at the inlet and at the compressor discharge. The losses in the inducer, the impeller and in the diffuser are predicted by applying empirical loss correlations. The difficulty in using empirical loss models is that they need validation; often their parameters need to get calibrated and are indirectly a function of the impeller geometry, power and gas properties. Well calibrated design tools are very rapid and are successfully being applied in large industrial companies, that have managed (over the years) to build a large empirical database. Keskin and Bestle [35] have used the Rolls-Royce tools for successfully optimizing a multi-stage axial compressor. In order to get hold of a basic layout tool it was decided to build a model based on available loss models successfully used in larger impellers. The validation and the calibration would require a prototype and measured data, of course.

The general one-dimensional design procedure is standard and is detailed in several text books. The development of the one-dimensional model is inspired by the procedure described by Whitfield and Baines [36] proposing to model each component of the compressor stage separately in the direction of the flow, each component (or section) being defined by an inlet and a discharge surface. Depending on which part one is modeling, different loss correlations are imposed between the inlet and the discharge section. As the general procedure for calculation is well known the following paragraphs will concentrate on the losses

incurring in the several stage components and the corresponding models used.

3.1. The inducer

The inducer region is characterized by a straight, axial flow in a stationary duct (no inlet guide vanes). The stagnation pressure loss due to wall friction of a turbulent, incompressible flow in a duct is given in any fluid mechanics text and can be modeled as follows:

$$p_{0in} - p_{0out} = \frac{4C_f \rho l w^2}{2D_h} \quad (1)$$

where C_f is the friction coefficient that is dependent on the local Reynolds number as well as on the relative pipe wall roughness. The friction coefficient is calculated according to Moody [18]. L is the pipe length, D_h the hydraulic diameter and w the flow velocity. In general, the velocity in the inducer duct is low enough ($Ma < 0.4$) to allow the assumption of incompressible flow.

3.2. The impeller

The impeller passage corresponds to a rotating duct. It is characterized by internal and by external losses. Internal ones affect the exhaust pressure and increase the entropy in the system. External losses only increase the required enthalpy but do not affect the exhaust pressure.

The incidence losses are calculated by using a technique developed by Galvas [37]. The method consists in specifying an incidence angle at which the incidence losses are minimum. The

deviation from the optimum angle leads to a perpendicular velocity deviation that is being lost. The corresponding loss in enthalpy can be expressed as follows:

$$\Delta h_{inc} = \frac{1}{2} [w_{in} \sin(|\beta_{in} - \beta_{opt}|)]^2 \quad (2)$$

The skin friction losses are generated by the viscous shear forces in the boundary layers. Both Jansen [19] and Coppage et al. [38] used the expression for pipe flow losses for calculating the friction losses:

$$\Delta h_{sf} = \frac{4C_f L_h \bar{w}^2}{2D_h} \quad (3)$$

where \bar{w} is the average relative velocity, D_h and L_h the hydraulic diameter and channel length. An expression for the latter is given by Galvas [37].

The diffusion and the blade loading losses are due to the boundary layer growth and separation as well as to secondary flow development and seem to be characterized by a diffusion coefficient. Rodgers [39,40] investigated the influence of the diffusion factor on the impeller efficiency and proposed the following expression for characterizing the losses:

$$\Delta h_{bl} = 0.05 D_f u_t^2 \quad (4)$$

where

$$D_f = 1 - \frac{w_4}{w_{2rms}} + \frac{\pi r_4 \Delta h_{is}}{N_{BL} L_h u_t w_{2rms}} + 0.1 \frac{r_{2s} - r_{2h} + b_4}{2(r_4 - r_{2s})} \left(1 + \frac{w_4}{w_{2rms}} \right) \quad (5)$$

For the clearance losses Senoo and Ishida [22] presented measured data showing that the losses due to the clearance decreased with increasing pressure ratio. Brasz [23] showed that the losses increase non-linearly with the tip clearance; the efficiency drops more rapidly at low than at high relative clearances. He proposed the following expression for modeling the losses due to the tip clearance:

$$\Delta h_{cl} = 0.6 \frac{e_{tip}}{b_4 + \frac{e_{tip}}{2}} C_{\theta 4} \sqrt{\frac{4\pi C_{\theta 4} C_{m2}}{(b_4 + \frac{e_{tip}}{2}) N_{BL}} \left[\frac{r_{2s}^2 - r_{2h}^2}{(r_4 - r_{2s}) \left(1 + \frac{\rho_4}{\rho_2} \right)} \right]} \quad (6)$$

The internal losses described above are added up and the gain in entropy, or the loss in total pressure is calculated iteratively when performing the calculation of the impeller exhaust properties. In opposition to the internal losses the external ones increase the required enthalpy to perform the compression, however, without affecting the exhaust pressure.

The disc friction losses are generated by the shear flow forces at the impeller backplate. The most common approach is given by Daily and Nece [41] who based their model on experimental data. The enthalpy rise due to disc friction is given as follows:

$$\Delta h_{df} = 0.25 \rho_4 u_t^3 r_4^2 K_f \frac{1}{m} \quad (7)$$

where

$$\begin{aligned} K_f &= 3.7 \left(\frac{e_{back}}{r_4} \right)^{0.1} Re^{-0.5} \quad Re < 3 \cdot 10^5 \\ K_f &= 0.102 \left(\frac{e_{back}}{r_4} \right)^{0.1} Re^{-0.2} \quad Re > 3 \cdot 10^5 \end{aligned} \quad (8)$$

with

$$Re = \frac{u_t \rho_4 r_4}{\mu_4}$$

The recirculation loss is represented by the work performed on the portion of the fluid flow that does not have enough momentum to flow against the pressure gradient in the diffuser and flows back into the impeller. Coppage et al. [38] models these losses as a function of the absolute exit flow angle and of the diffusion coefficient defined in Eq. (5). The recirculation losses are expressed as follows:

$$\Delta h_{rc} = 0.02 D_f^2 u_t^2 \tan \alpha_4 \quad (9)$$

3.3. The vaneless diffuser

The flow in the vaneless diffuser is characterized by being both unguided and swirling. Stanitz [42] developed an analysis method for one-dimensional, compressible flow including skin friction, heat transfer and area change in vaneless diffusers. The analysis does not include inlet flow non-uniformities and is based on the continuity and on the momentum equations. The skin friction losses are modeled in a similar way as in Eq. (3) using a friction coefficient C_f . Japikse [43] performed extensive tests with vaneless diffusers and proposed a friction coefficient as follows:

$$C_f = k \left(\frac{1.8 \cdot 10^5}{Re} \right)^{0.2} \quad (10)$$

where k is often given the value of 0.01. Japikse points out that there are also measurements suggesting values of 0.005 or even 0.02. The equation system as defined by Stanitz is being solved iteratively.

A further concern related to the diffuser, is its stability. As a matter of fact if the flow rate falls below a critical rate, stall or even surge may appear. Jansen [44] has analyzed the theoretical and the experimental aspects of this unsteady flow. He showed that the rotating stall is triggered by a local inversion of the radial velocity component in the diffuser. He proposed that the onset of rotating stall is dependent on the absolute flow angle, the inlet Reynolds number, the inlet Mach number and on the diffuser width. Later Senoo and Kinoshita [45] further investigated the onset of the instability. They presented a correlation for a critical flow angle at which the reverse flow commenced. They further correlated the critical angle (α_{4r}) to the diffuser width ratio (b_4/r_4) and to the inlet Mach number. In addition they investigated the impact of the inlet flow distortion: a radial flow distortion of 0.3 leads to a reduction of the critical angle by approximately 5 degrees. A comparison of theoretical and experimental data led them to a definition of a critical flow angle (α_{4c}) at which rotating stall begins [46]:

$$\frac{90 - \alpha_{4c}}{90 - \alpha_{4r}} = 0.88 \quad (11)$$

3.4. The volute

In general, after the diffuser, the flow is led to a tangential exhaust pipe by using a scroll volute. A model based on incompressible flow has been given by Japikse [47]. The losses are calculated on two assumptions:

1. The meridional component of the kinetic energy of the flow entering the scroll is totally lost.
2. If the tangential flow entering the scroll accelerates then no additional losses occur. If the tangential flow decelerates, then the flow diffuses and the total pressure loss is calculated like a sudden expansion loss.

The assumptions allow to express the pressure loss coefficient related to the volute as follows:

$$K_L = \frac{0.6}{1+\lambda^2} \quad \lambda A_{7/5} \geq 1$$

$$K_L = \frac{0.6}{1+\lambda^2} + 0.5 \frac{(\lambda - 1/A_{7/5})^2}{\sqrt{1+\lambda^2}} \quad \lambda A_{7/5} < 1$$

where

$$K_L = \frac{p_{05} - p_{07}}{p_{05} - p_5} \quad (12)$$

$$A_{7/5} = \frac{\pi d_7^2/4}{2\pi r_5 b_5} \quad (13)$$

$$\lambda = \frac{c_{\theta 5}}{c_{m5}} = \tan \beta_5 \quad (14)$$

where the subscript 5 defines the location at the diffuser discharge and 7 the exhaust of the volute. d_7 corresponds to the exhaust diameter of the volute after the tongue.

3.5. The computer program

A computer program was generated in Matlab allowing to calculate the compressor pressure ratio and isentropic efficiency for a given impeller geometry, mass flow and rotational speed. The one-dimensional design procedure was implemented using the loss correlations described. As the compressor is likely to operate very close to saturation, the perfect gas assumption is not valid. Therefore the thermodynamic properties are calculated through Refprop [48] using a Matlab interface (called FLINT) developed inhouse. In order to be able to predict the onset of rotating stall the curves for the critical flow angle in Senoo's papers [45,46] were interpolated. Tests for choke are implemented at each station and if the flow is blocked the calculation is stopped. The output function for the complete compressor stage model can be expressed as follows:

$$[\Pi, \eta_{is-k}, \text{Choke}, \text{Surge}] = f_K(\text{Geometry}, \dot{m}, N_{rot}) \quad (15)$$

The geometry parameters affecting the performance and the operational range of the compressor stage are given in Fig. 2.

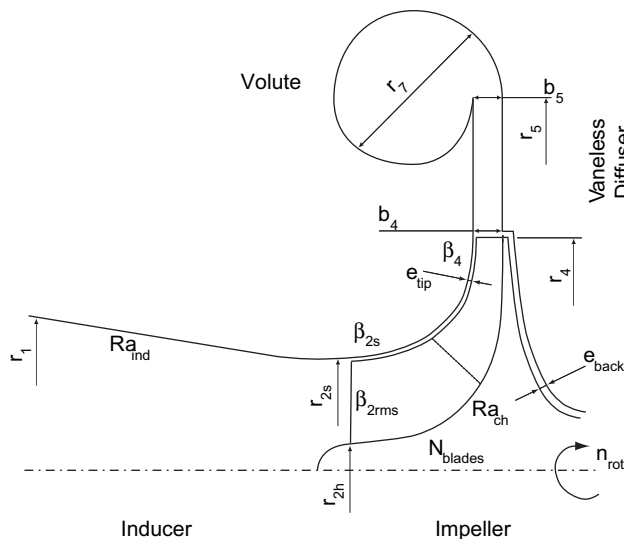


Fig. 2. The geometry description of a compressor stage with no inlet guide vanes and with a vaneless diffuser.

4. Experimental validation

In order to be able to test the impeller initially designed (see Section 2) and to validate the compressor model described above, a hermetic testrig has been designed. The testrig is composed of the main refrigerant cycle through which the major portion of the flow is conveyed, and of a secondary cycle that provides the bearing section with clean and filtered vapor phase refrigerant. A detailed overview of the layout of the testrig is given in Fig. 3. The compressor unit, an electronically controllable expansion valve, a heat exchanger and a separator are part of the main cycle. The energy brought into the cycle through the compressor is dissipated by the heat exchanger. Partially filled with liquid refrigerant, the heat exchanger stabilizes the compressor's inlet pressure. Therefore the pressure level of the compressor intake is controlled through the temperature of the cooling liquid. Both, the rotational speed of the compressor unit and the position of the electronic expansion valve allow to control the exhaust pressure and the mass flow of the compressor. The auxiliary bearing supply cycle taps high pressure refrigerant after the mass flow measurement, and drives it around the bearings. To ensure cleanliness in the bearing section the tapped refrigerant is filtered. An additional external circuit provides for the cooling of the electric motor of the compressor unit. A detailed overview of the testrig components is given in Table 3. Temperature, pressure and mass-flow probes allow to measure the thermodynamic properties at the inlet and at the exhaust of the compressor and enable the calculation of the performance of the compressor system. Table 4 gives an overview of the probes installed on the testrig. Table 5 represents the type of transmitters, their calibration range and precision. The pressure and the

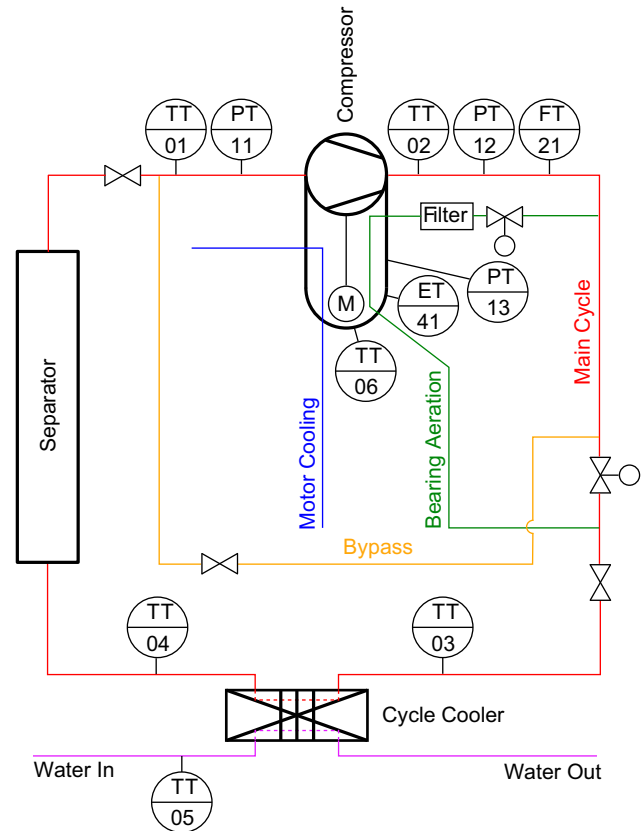


Fig. 3. The schematic representation of the vapor phase testrig showing the main components and the location of the pressure, temperature, displacement, mass-flow and power measurements.

Table 3

The complete list of the components of the testrig.

Cooler	SWEP	B8 × 10HP
Filter	Swagelock	SS-2F-05
Expansion valve	Sporlan	SDR4 10'-S
Micro valve	Swagelock	B-2MG-EP
Ball valve	Mueller	FP-35224
Ball valve	Mueller	F-35223
Copper fittings	Mueller	
Bypass valve	Swagelock	SS-43TS4

temperature probes have been calibrated on the indicated range. The other probes were delivered with calibration certificates. The error propagation is approximated by the first order Taylor series. Suppose a performance N being a function of several measurements u_i ($N = F(u_1, u_2, \dots, u_n)$), then the measurement error on the performance comes to:

$$\Delta N = \sum \left| \Delta u_i \frac{\partial f}{\partial u_i} \right| \quad (16)$$

The internal efficiency of the compressor can be expressed as follows:

$$\eta_{is-k} = \frac{e_{is}}{e_{meas}} \quad (17)$$

where e_{is} is a function of T_{in} , p_{in} and of p_{out} . On the other hand e_{meas} is a function of T_{in} , p_{in} and of T_{out} and p_{out} . As the compressor is operating close to the saturation line the energies have to be calculated using the real gas database. The consequence is that the derivatives required for estimating the measurement error have to be calculated numerically. The probes are scanned by two synchronized PCMCIA data acquisition boards, a rapid one for the pressures, the mass flow as well as for the electric power measurement and a slow one for the temperatures. A LabView Virtual Instrument (VI) has been used for the visualization of the measured data. The VI allows to plot the evolution of the different thermodynamic measurements as function of time and of the rotational speed. It further plots the measured compressor map and allows to control the electronic expansion valve.

Fig. 4 represents the measured and the predicted compressor map with the inlet conditions corresponding to the OP A-12, measured at rotational speeds between 170 and 210 krpm reaching a maximum pressure ratio of 3.27. The predicted compressor map was drawn using the 1D-model developed in Section 3. The prediction on the pressure ratio is within $\pm 5\%$ on the whole range. The major error occurs close to surge at the maximum pressure ratio. The model predicts the onset of surge at higher mass flows. Note, however, that the measurement of the onset of aerodynamic instabilities in the diffuser were not possible with the present equipment. It is therefore likely that instabilities occurred when the

Table 4

The listing of the different measurements and the corresponding probes.

Pos	Measurement of	Unit	Probe
01	Inlet Temp. Comp.	[°C]	Thermocouple Type K
02	Exh. Temp. Comp.	[°C]	Thermocouple Type K
03	Inlet Temp. Cooler Refr.	[°C]	Thermocouple Type K
04	Exh. Temp. Cooler Refr.	[°C]	Thermocouple Type K
05	Inlet Temp. Cooler Water	[°C]	Thermocouple Type K
06	Motor Temp.	[°C]	Thermocouple Type K
11	Inlet Pressure	[MPa]	Kistler A5
12	Exhaust Pressure	[MPa]	Kistler A20
13	Bearing Pressure	[MPa]	Kistler A20
21	Mass-flow	[kg s ⁻¹]	Micro Motion F050, El. 1700
41	Electric Power	[kW]	Norma D5155

Table 5

The precision of the different measurement probes.

Measurement	Type of probe	Range (calibration)	Precision
Temperature	Thermocouple Type K	[−20 to 50 °C]	±0.2 K
Pressure	Piezo-Resistive	[0.1 – 1 MPa]	±0.002 MPa
Mass-flow	Coriolis force	[0–0.1 kg s ⁻¹]	±0.5%
Electric Power	V-A measurement	[0 – 5 kW]	±0.1%

measurements of the characteristic were performed close to lowest mass flows. Fig. 5 represents the measured isentropic internal compressor efficiency corresponding to the compressor map in Fig. 4 and compares them to the predicted ones. The prediction underestimates the measured efficiency by 8 points at peak efficiency. The prediction is more accurate in the regions close to surge and to choke. Isentropic compressor efficiencies reaching 80% have been measured for the OP A-12, showing that the current 20 mm impeller design allows to reach excellent efficiency levels for pressure ratios up to 3.3 within a large mass-flow range. The good agreement between the compressor model developed in Section 3 and the measured data validates the model.

5. Single operating point optimization

When it comes to the design of a compressor stage all the variables describing the detailed geometry are basically free to move and may be included in the overall impeller geometry optimization. Obviously the geometric variables influence the compressor map. Some of them, however, are known to have little impact on the optimum value of other variables, such as the leading edge blade angle. Others are fixed by external constraints, such as the tip clearance, the blade channel roughness or the backplate clearance, to name a few.

Table 1 summarizes the different operational points required by the heat pump application. In order to emphasize the extend of the operational range required by the heat pump the impeller geometry has been optimized for maximum efficiency for each operation point separately. The mathematical form of the optimization process can be summarized as follows:

$$\begin{aligned} [\max(\eta_{is-k_i}), \max(N_{rot_i})] &= f_K(Geom, OP_i) \\ [\max(\eta_{is-k_i}), \min(N_{rot_i})] &= f_K(Geom, OP_i) \end{aligned} \quad (18)$$

subject to:

$$\begin{aligned} \text{Surge} &= 0 \\ \text{Choke} &= 0 \end{aligned}$$

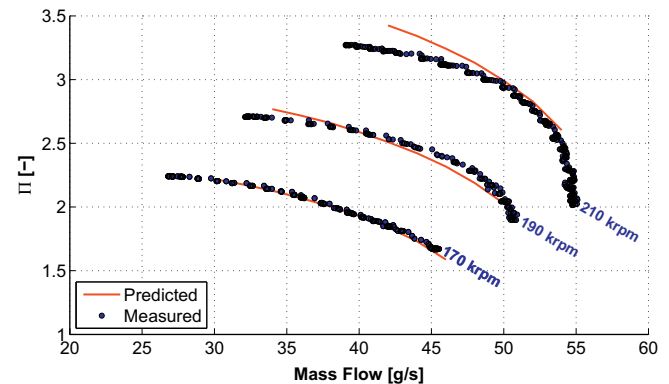


Fig. 4. Comparison between the measured and the predicted compressor map corresponding to the inlet condition of OP 1.

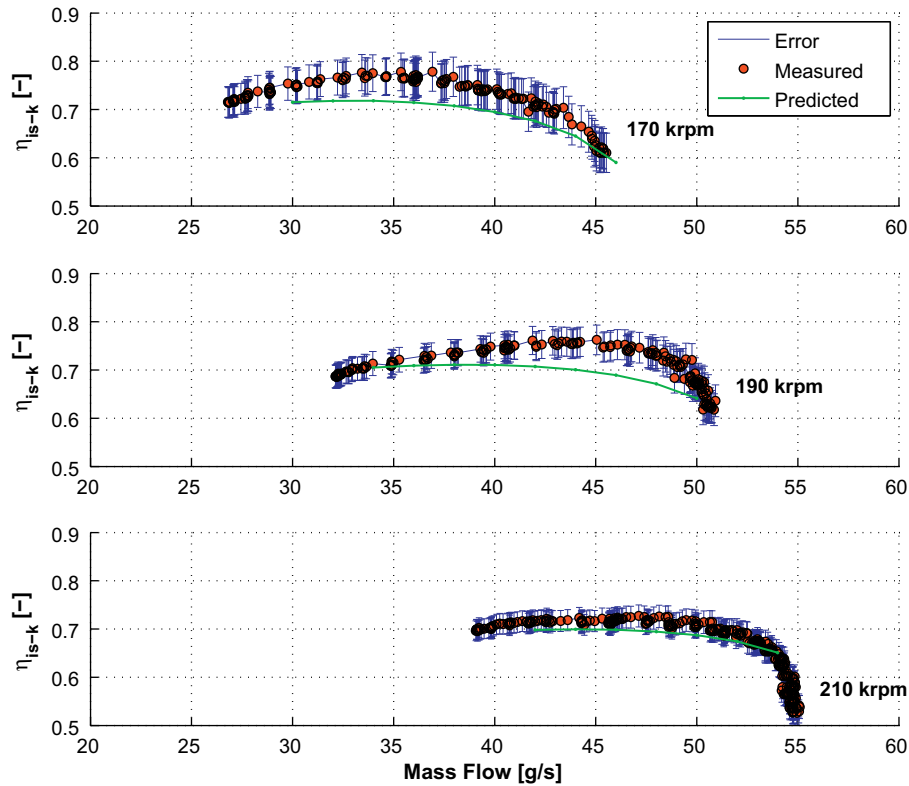


Fig. 5. Comparison between the measured and the predicted isentropic compressor efficiency corresponding to the map in Fig. 4.

The rotational speed has been once minimized and once maximized in order to be able to express the evolution of the efficiency and corresponding geometrical dimensions as a function of the rotational speed.

The optimization process itself is performed using an Evolutionary Algorithm, MOO, which has been developed by Leyland [49] and Molyneux [50]. This kind of algorithm is based on heuristic methods and allows to cover the exploration of the whole space delimited by the decision variables, even if the solution space is non linear and/or non contiguous. Compared to gradient-based approaches the advantage of the Evolutionary Algorithms is that the search for solutions is truly global within the variable's space on the one hand and insensitive to the initial starting point on the other.

The optimization process was started with a random population of 500 individuals and stopped after 100,000 evaluations. The optimizing function includes surge by a penalization function that decreases the efficiency exponentially the deeper the solution travels in surge. When choke appears at any stage, the calculations stop, and a pressure ratio of -1 and an efficiency of 0 are attributed. This potential step in the objective function values is not of advantage as the optimizer has difficulties to understand how to handle such discontinuities. The optimizer does not fail but it takes longer to converge. Table 6 indicates the fixed geometry values and the range of the variables included for the optimization. Fig. 6 represents the pareto optimum efficiency as a function of rotational speed for each operation point. Accordingly the optimum rotational speeds range from approximately 100–300 krpm for the five operation points. The corresponding major geometrical dimensions of the different solutions are given in Fig. 7 as a function of the specific speed for each operational point. The optimum impeller for the operation point A-12 would have a tip diameter of approximately 20 mm and tip width (b_4) of 0.8 mm rotating at 120 krpm

whereas the optimum impeller for the point A12 would have a diameter of 8 mm and a tip width of 0.3 and rotate at 300 krpm. The convergence on the exit blade angle β_4 is rather difficult. The reason is that the influence of β_4 does not weight as much as the other geometrical dimensions. An optimization performed with a fixed $\beta_4 = -45^\circ$ has resulted in a considerably more rapid convergence and in a peak efficiency lower by 0.5 points. As a tendency, however, the exit blade angle around the optimum for each operational point is rather high, whereas the angle decreases with increasing as well as with decreasing rotational speed. The main influence of the exit blade angle is rather on the width of the compressor map. As a matter of fact the mass-flow range between surge and choke increases with decreasing β_4 . As the impellers are

Table 6

The geometrical dimensions of the variables for the individual optimization of the impeller.

Inlet shroud radius	r_{2s}/r_{2h}	[m]	$\in [0.2-0.4]$
Inlet hub radius	r_{2h}/r_4	[-]	$\in [0.015-0.8]$
Tip radius	r_4	[m]	$\in [0.002-0.035]$
Tip width	b_4/r_4	[m]	$\in [0.015-0.3]$
Blades	N_{Bl}	[-]	$\in [5-11]$
Tip blade angle	β_4	[°]	$\in [-45-0]$
Inducer inlet radius	r_1	[m]	$1.1 \times r_{2s}$
Inducer Length	L_{ind}	[m]	$4 \times r_4$
Diffuser exit radius	r_5	[m]	$1.5 \times r_4$
Tip clearance	e_{tip}	[m]	$0.2 \times r_4^2$
Backface clearance	e_{back}	[m]	$0.05 \times r_4$
Diffuser exit width	b_5	[m]	b_4
Splitter Blades	N_{Sp}	[-]	N_{Bl}
Inlet blade angle shr	β_{2s}	[°]	-60
Blade thickness	e_{blade}	[m]	2×10^{-4}
Inducer Roughness	Ra_{ind}	[m]	1.2×10^{-5}
Impeller Roughness	Ra_{ch}	[m]	1.2×10^{-5}
Gas			R134a

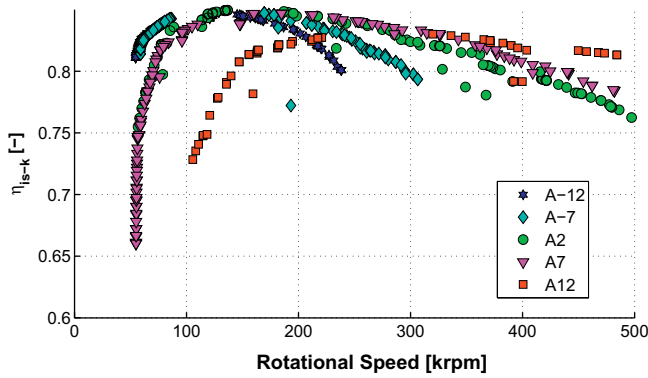


Fig. 6. The maximum isentropic efficiency as a function of the rotational speed for each operational point resulting from the optimization of the impeller geometry.

optimized for one operation point only, as if they would operate at only one nominal point, this fact is not taken into account yet. The reason that some of the curves are not continuous at some points does not result from bad convergence but rather from the fact that the number of blades is integer.

The large difference in optimum rotational speeds and dimensions emphasizes the difficulty in meeting the heat pump requirements with a single impeller. A joint optimization of all the operational points will show if the requirement to reach all the points is not too stringent. It is interesting to note that the ratio between the different impeller sizes and the tip radius do behave in a similar manner as function of the rotational speed, independently of the operation point. As a matter of fact for speeds lower than the optimum the impeller has a large tip radius (r_4), a relatively small inlet shroud radius (r_{2s}) and tip width (b_4), whereas at higher speeds the tip radius becomes smaller and the relative tip width and inlet shroud radius larger. The diameter of the wheel decreases

with speed as the pressure ratio is basically defined by the tip speed. The tip width increases with speed as the discharge surface of the impeller has to remain constant for a given mass flow.

In order to understand why there is a rotational speed at which the efficiency reaches a maximum, the losses for the operation point A7 have been plotted as a function of the specific speed, visualizing their distribution (Fig. 8). As can be seen the total losses reach a minimum where the efficiency is maximum. The internal losses, composed of incidence at the leading edge, diffusion, skin friction and clearance losses, increase with increasing rotational speed, i.e. with decreasing tip radius. On the other hand the external losses, disc friction and recirculation losses, increase with increasing tip radius. A closer analysis of the internal losses reveals that the main driver for them is the skin friction. Except for very low rotational speeds all the internal losses increase with rotational speed or with decreasing tip radius. The reason is that the main drivers for internal losses are the amplitudes of the relative speeds at the leading edge and at the tip of the impeller (see eqs. (2)–(6)). As the mass flow has to remain constant at a given OP the relative speed has to increase if the impeller size and therefore the cross-section of a blade channel decrease. The external losses are characterized by very high disc friction losses at low speeds, i.e. at large tip radius but decrease rapidly with decreasing wheel diameter.

In terms of the total losses the two main drivers are skin and disc friction. Skin friction increases with decreasing tip diameter and with increasing rotational speed whereas disc friction is basically dependent on the tip diameter and therefore the main source of losses for large impellers rotating at low speeds. The only efficient way to decrease skin friction is the reduction of the channel roughness. Disc friction is driven by the tip radius and to a lower extent by the gap from the wheel to the impeller backplate. The actions on the disc friction are limited.

A further interesting result is given by the fact that the three OPs A-12, A-7 and A2 reach similar maximum efficiencies (around 85%) whereas the optimum solutions for OP A7 and especially A12 are

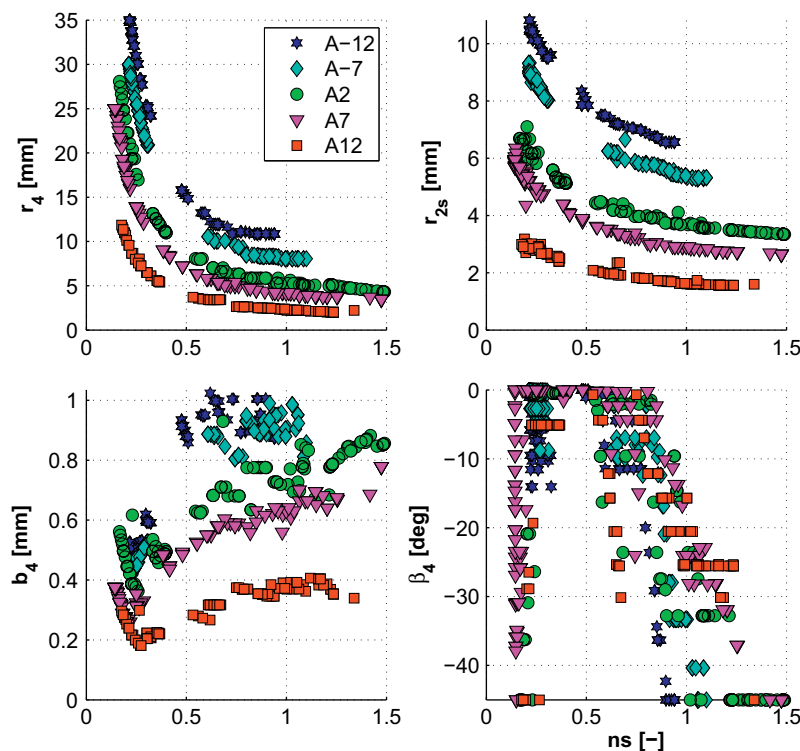


Fig. 7. The major impeller dimensions as a function of the specific speed for each operational point as a result of the optimization.

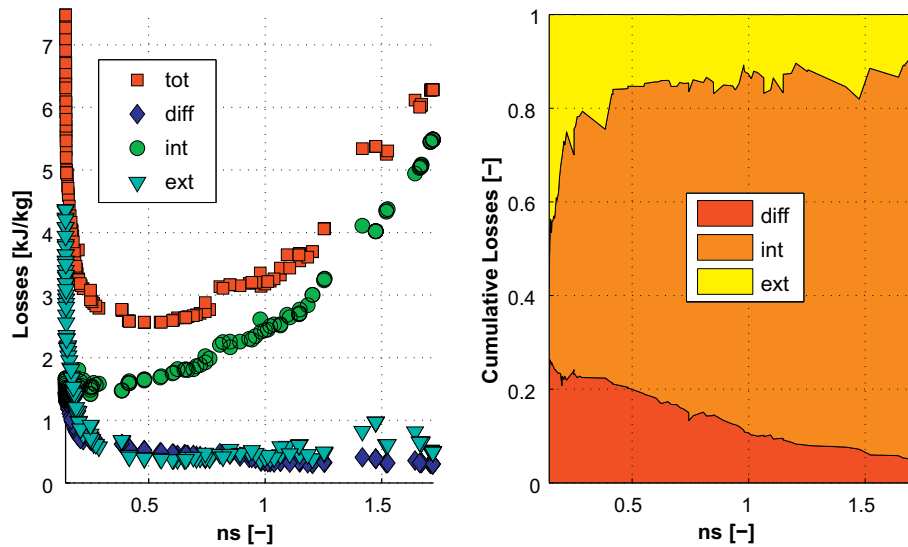


Fig. 8. The external, the internal and the diffuser losses as a function of the specific speed for the operation point A7.

apparently not able to reach as high efficiencies as the impellers for the OPs with higher pressure ratios. This is somewhat surprising as intuitively it should be easier to reach low pressure ratios. The reason is given by a simple analysis of the Reynolds number. As a matter of fact the mass flows for the OPA7 and even more A12 are low enough to lead to small impellers with Reynolds numbers that are already in the transition zone, resulting in comparatively high skin friction coefficients.

6. Multiple operating point optimization

After having optimized the impeller for each OP individually the next step is the optimization of the impeller geometry not just for one operation point but for all of them simultaneously such that the impeller satisfies the requirements of the heat pump on the complete operational range, as far as possible. What has to be optimized in this case is not primarily the efficiency of the compressor stage at each OP but rather the energy consumption of the compressor over the heating season. The total energy consumption can be expressed as follows:

$$E_{el} = \sum_{T_{ext}} \frac{e_{is}(T_{ext}) \dot{m}(T_{ext})}{\eta_{is-k}(T_{ext})} n_d(T_{ext}) \cdot 24 \cdot 3600 \quad (19)$$

where e_{is} is the isentropic energy, \dot{m} is the mass flow, η_{is} the isentropic efficiency and n_d is the number of days at which the temperature T_{ext} occurs. The overall seasonal compressor efficiency can be expressed as follows:

$$\eta_{y-k} = \frac{\sum e_{is}(T_{ext}) \dot{m}(T_{ext}) n_d(T_{ext})}{\sum \frac{e_{is}(T_{ext}) \dot{m}(T_{ext})}{\eta_{is-k}(T_{ext})} n_d(T_{ext})} \quad (20)$$

In order to be able to calculate the number of days at a certain temperature the climatic conditions in which the heat pump is operating have to be known. The daily average temperature occurrence of a large number of cities worldwide is continuously updated and provided by the University of Dayton [51]. Fig. 9 shows the temperature frequency expressed in days per year measured in Zuerich (Switzerland). The data gets distributed into bins corresponding to the five operation points and the number of days for each bin is then calculated accordingly. The climatic temperature distribution in Zuerich leads to the conclusion that 47% of the

seasonal energy consumption (for heating purpose only!) is covered by the operation point A2. More than 70% are contained by the operation points A2, A7 and A12 and 96% by A-7, A2 and A7. This emphasizes the fact that the 3 intermediate OPs are the most important in terms of overall energy consumption.

First it was tried to optimize the impeller for all the five OP simultaneously, leading, however, to no viable solutions. It follows that no solution seems to be possible that incorporates all the requirements. The mass flow for OP A12 is too low and the one for OP A-12 is too high, leading either to surge at A12 or to choke at A-12, whatever the geometry of the impeller was. Following the fact that 96% of the required heating energy was contained by the points A-7, A2 and A7 the impeller was optimized for the 3 intermediate OPs at the same time. OP A12 is not critical as the impeller is being optimized for higher pressure ratios, i.e. the impeller will be able to deliver the required pressure ratio but is likely to deliver too much mass flow and therefore too much heating power, leading to an intermittent operation of the heat pump. OP A-12 is more critical as the required pressure ratio is the highest, and it would be theoretically possible that the optimization would lead to a family of solutions that does not allow to reach OP A-12 in term of the pressure ratio. What is more likely, however is that the solutions will reach the pressure ratio of 4.17 but not the required mass flow. In such a case the heat pump would not be able to supply enough

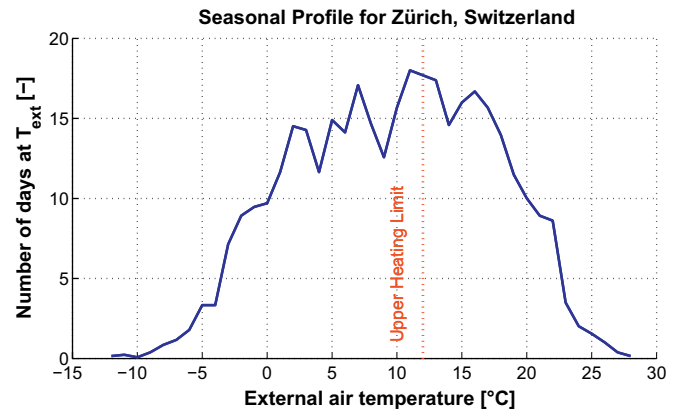


Fig. 9. The seasonal climatic temperature distribution in Zuerich, Switzerland.

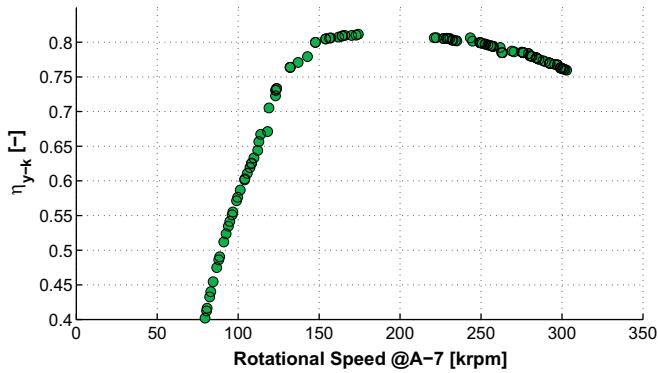


Fig. 10. The pareto optimum yearly energy efficiency as a function of the maximum required rotational speed (OP 2).

heat. The remainder would have to be delivered by another source. This is not a real issue as the occurrence of OP A-12 is very low. The optimization can be expressed as follows:

$$\begin{aligned} \left[\max(\eta_{y-k}), \max(n_{rot}) \right] &= f_K(Geom, OP_i) \\ \left[\max(\eta_{y-k}), \min(n_{rot}) \right] &= f_K(Geom, OP_i) \end{aligned} \quad (21)$$

subject to:

$$\begin{aligned} \text{Surge} &= 0 \\ \text{Choke} &= 0 \\ i &= 2, 3, 4 \end{aligned}$$

where η_{y-k} is given by Eq. (21). The optimization variables are summarized in Table 6.

After the optimization process, the choke limit for the impeller solutions on the pareto optimum operating at the OP A-12 was calculated in order to check first if the impellers were able to meet the required mass flow and secondly to define the maximum required rotational speeds for reaching the pressure ratio corresponding to the OP A-12. Fig. 10 shows the optimized yearly energy efficiency expressed for the 3 intermediate OP as a function of the rotational speed required to reach OP A-7, whereas Fig. 11 represents the rotational speeds required for reaching the required pressure ratios for the different OPs as a function of the pareto optimum tip radius as well as the choked mass flow at the OP A-12

and the mass flow at surge for the OP A12 as a function of the required rotational speed for reaching the pressure ratio of 4.17. With increasing tip radius the choked mass flow increases, for some solutions reaching even higher mass flows than the required 0.053 kg s^{-1} , at the expense however, of a considerable reduction of the overall yearly efficiency. The mass flow at OP A12 is considerably higher than the required 0.005 kg s^{-1} . The heat pump will have to operate in an on-off mode at this OP. For lower air temperatures, i.e. for OPs A7, A2 and A-7 the heat pump will continuously run and deliver exactly the required heat. At lower temperatures (A-12) not enough heat will be conveyed, the remainder will have to be either delivered by another source (electric resistances, wood furnace...) or if the cool period is short enough it will be damped by the thermal inertia of the house.

Although A-12 requires a higher pressure ratio than A-7, solutions with small tip radius require lower rotational speeds. The reason behind this curiosity lies in the exhaust pressure of the compressor stage. As a matter of fact it remains constant, whereas the inlet pressure decreases with decreasing external air temperature, leading to a situation where the choke at OPs with lower air temperatures appears rather in the inducer region than elsewhere. This means that the optimizer just manages to fit the OP A-7 close to the choke line and the OP A7 close to the surge line leaving very little margin for higher mass flows. Further decreasing the inlet pressure shifts the choke line toward lower mass flows. Due to the negative slope of the compressor characteristic resulting from negative exhaust blade angles, a shift toward lower mass flows increases the pressure ratio for a given rotational speed. Therefore the best solution for increasing the mass-flow range would be to increase the inducer section. According to the optimization this would be possible at the expense of efficiency, mainly due to increased diffusion losses.

The optimization loop maximizing the rotational speed leads to a narrower speed range than the one resulting from minimizing the speed. The reason lies in the size of the resulting impeller: higher rotational speeds require smaller impellers, leading (for a given mass flow) to an increased level of the relative speeds in the blade channels and therefore to a narrower range before reaching choke. Fig. 12 shows the efficiencies for each pareto optimum impeller expressed for the individual OPs as function of the required rotational speed, and compares them to the optimum impellers resulting from the individual OP impeller geometry optimization loops. For the OP A7 the resulting impeller would rotate at the

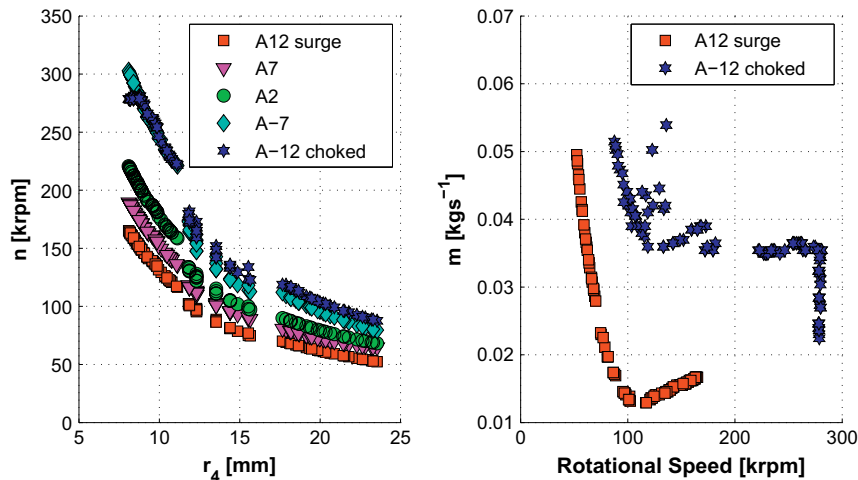


Fig. 11. The required rotational speeds as a function of the Pareto optimum tip radius, expressed for the different OPs and the mass flow at choke for the OP 1 and at surge for the OP 5 as a function of the required rotational speed.

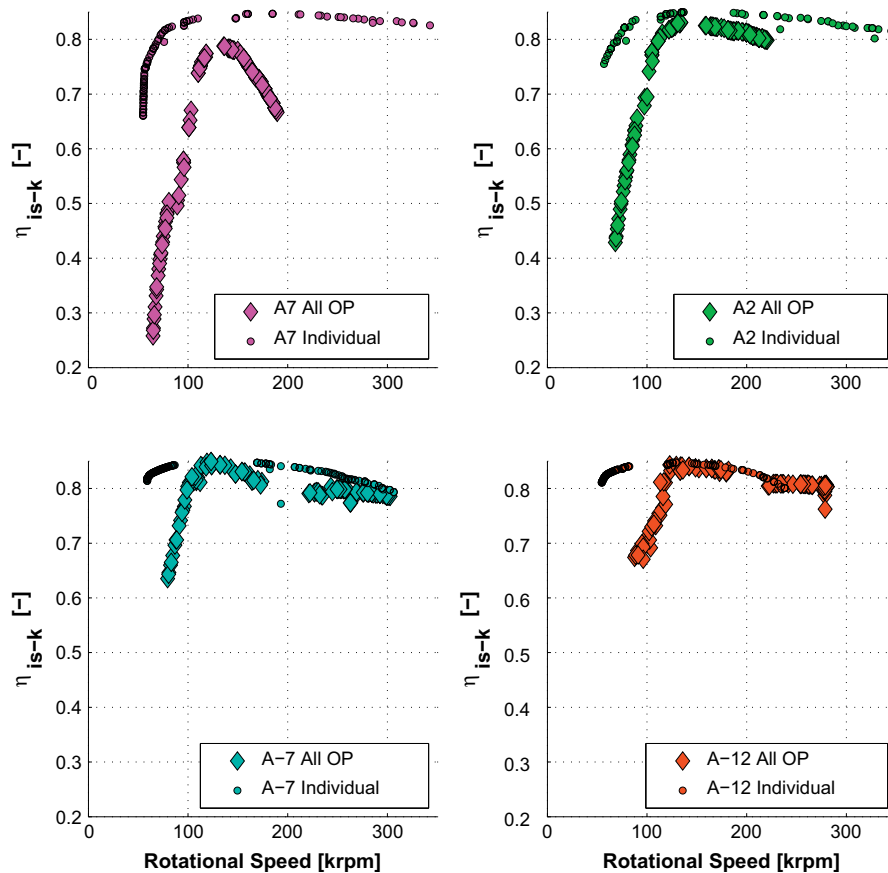


Fig. 12. The pareto optimum isentropic impeller efficiency as a function of the required rotational speed for each continuously operating OP compared to the evolution of the efficiency reached for an impeller optimized for each OP individually

correct speed, the geometry, however, is sub-optimal leading to a lower efficiency. For both the OPs A-7 and A-12 the rotational speed is too high leading to efficiencies lower than possible. As expected for the OP A2 the match is rather good, the efficiency is just slightly lower and the rotational speed corresponds to the optimum one resulting from the individual optimization. The simultaneous optimization of the 3 OPs has led to an impeller geometry that best fits the OP A2 as it is the one for which the

impact on the energy consumption is maximum. A closer analysis of the results, however, brings to evidence that the optimizer is more concerned about fitting the 3 OP between the choke and surge, rather than about the weight of the different OPs, resulting from the local climatic conditions. Fig. 13 represents the compressor maps for the three OPs for the optimum solution showing the required pressure ratios and mass flows (star). The OP A7 is operating on the verge of surge whereas OP A-7 operates in

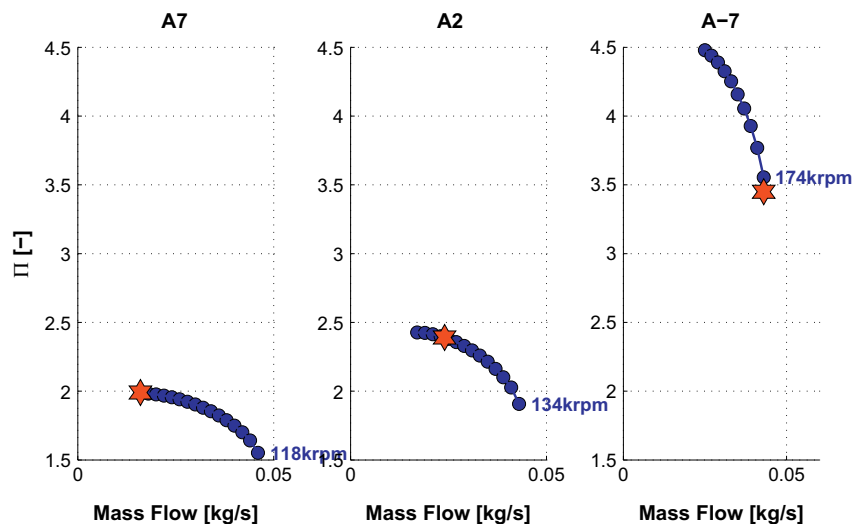


Fig. 13. The compressor maps for the optimum solution drawn for the three OPs 4, 3 and 2.

a nearly choked regime. It becomes evident that the three intermediate OPs are distant from each other in terms of mass flows and pressure ratio leaving the optimizer little margin for letting the climatic weight have a lot of effect. For considerably milder climatic conditions the optimization would have to include A12 rather than A-7, whereas for colder weather profiles A7 would have to be dropped in favor for A-12. Of course, these optimizations would lead to different optimum impeller geometries and rotational speeds. The compressor for milder temperatures is likely to become smaller and rotating faster, whereas the compressor for colder weather profiles would require larger impellers rotating at slower speeds.

7. Conclusion

The main driver for small scale turbomachinery in low power heat pumps is the potential for reaching higher efficiencies than volumetric compressors currently used in these machines and the potential for making the compressor oil-free, which bears a considerable advantage in the design of advanced multi-stage heat pump cycles. An appropriate turbocompressor for driving domestic heat pumps with a high temperature lift requires the ability to operate on a wide range of pressure ratios and mass flows. The designer is confronted with the necessity of a compromise in terms of range and efficiency. The present publication shows a possible way to deal with that difficulty, by coupling an appropriate and rapid modeling tool to a multi-objective optimizer. The advantages of that tool have been demonstrated on the example of the design of a single stage radial compressor. The optimizer manages to fit the compressor design into the possible specifications field while keeping the high efficiency on a wide operational range.

The 1D-tool used for the compressor stage modeling has been validated by experimentally testing an initial impeller design. The good agreement between the model predictions and the measured data validates the simple model, allowing its use for further design.

The excellent experimental results, the good agreement with the model and the linking of the model to a multi-objective optimizer will allow to design radial compressor stages managing to fit the wide operational range of domestic heat pumps while keeping the efficiency level very high.

Acknowledgements

The authors would like to thank the Fischer Precise Group for their support of this work and for the permission to publish this paper.

References

- [1] IEA. Renewables for heating and cooling. International Energy Agency; 2007.
- [2] Favrat D, Maréchal F, Epelly O. The challenge of introducing an exergy indicator in a local law on energy. *Energy* 2008;33(2):130–136.
- [3] Burer M, Favrat D, Tanaka K, Yamada K. Multicriteria optimisation of a district heating cogeneration plant integrating a solid oxide fuel cell-gas turbine combined cycle, heat pumps and chillers. *Energy* 2003;28(6):497–518.
- [4] Schiffmann J, Molyneaux A, Favrat D, Maréchal F, Zehnder M, Godat J. Compresseur radial pour pompe à chaleur biétagée, phase 1. Technical Report OFEN no. (SB) ENET 220195. Swiss Federal Office for Energy; 2002.
- [5] Schiffmann J, Favrat D. Experimental investigation of a direct driven radial compressor for domestic heat pumps. *International Journal of Refrigeration* 2009;. doi:10.1016/j.jirefrig.2009.07.006.
- [6] Higashimori H, Hasagawa K, Sumida K, Suita T. Detailed flow study of mach number 1.6 high transonic flow with a shock wave in a pressure ratio 11 centrifugal compressor impeller. *Journal of Turbomachinery* 2004;126(4):473–481.
- [7] Strong DTG. Development of directly fired domestic heat pump, PhD thesis. Oxford University; 1980.
- [8] Yun H, Smith JL. Centrifugal compressors for automotive air conditioners—component design, In: The 1996 ASME international mechanical engineering congress and exposition, Atlanta, USA; 1996. p. 115–122.
- [9] Mehra A, Jacobson SA, Tan CS, Epstein AH. Aerodynamic design considerations for the turbomachinery of a micro gas turbine engine. In: 25th national and first international conference on fluid mechanics & fluid power, New Delhi, India; 1998.
- [10] Frechette LG, Jacobson SA, Breuer KS, Ehrich FF, Ghodssi R, Khanna R, et al. Demonstration of a microfabricated high-speed turbine supported on gas bearings. In: solid-state Sensor and Actuator Workshop, Hilton head is, SC, USA; 2000.
- [11] Epstein AH. Millimeter-scale, micro-electro-mechanical systems gas turbine engines. *Journal of Engineering for Gas Turbines and Power* 2004;126(2):205–225.
- [12] Isomura K, Murayama M, Kawakubo T. Feasibility study of a gas turbine at micro scale. In: ASME Turbo Expo, New Orleans, Louisiana, USA; 2001 [ASME Paper 2001-GT-0101].
- [13] Johnston JP, Kang S, Arima T, Matsunaga M, Tsuru H, Prinz FB. Performance of a micro-scale radial-flow compressor impeller made of silicon nitride. In: International gas turbine congress, Tokyo, Japan; 2003 [IGTC2003 TOKYO OS-110].
- [14] Kang S, Johnston JP, Arima T, Matsunaga M, Tsuru H, Printz FB. Microscale radial-flow compressor impeller made of silicon nitride: manufacturing and performance. *Journal of Engineering for Gas Turbines and Power* 2004;126(2):358–365.
- [15] Isomura K, Murayama M, Teramoto S, Hikichi K, Endo Y, Togo S, Tanaka S. Experimental verification of the feasibility of 100 W class micro-scale gas turbine at an impeller diameter of 10 mm. *Journal of Micromechanics and Microengineering* 2006;16(9):254–261.
- [16] Sirakov BT. Characterization and design of a non-adiabatic micro-compressor impeller and preliminary design of self-sustained micro engine system, PhD thesis. Massachusetts Institute of Technology; 2005.
- [17] Casey MV. The effects of Reynolds number on the efficiency of centrifugal compressor stages. *Journal of Engineering for Gas Turbines and Power* 1985;107:541–548.
- [18] Moody LF. Friction factors for pipe flow. *ASME Transactions* 1944;66(8):671–684.
- [19] Jansen W. A method for calculating the flow in a centrifugal compressor impeller when entropy gradients are present. In: Royal Society conference on internal aerodynamics (turbomachinery); 1967. 133–146.
- [20] Pampreen RC. Small turbomachinery compressor and fan aerodynamics. *Journal of Engineering for Power* 1973;95:251–261.
- [21] Musgrave DS. The prediction of design and off-design efficiency for centrifugal compressor impellers. In: ASME 22nd fluids engineering conference, New Orleans, USA; 1980.
- [22] Senoo Y, Ishida M. Deterioration of compressor performance due to tip clearance on centrifugal compressors. *Journal of Turbomachinery* 1987;109:55–61.
- [23] Brasz JJ. Investigation into the effect of tip clearance on centrifugal compressor performance. In: ASME Gas Turbine and aeroengine congress and exposition, Amsterdam, Netherlands; 1988 [ASME-Paper 88-GT-190].
- [24] Gong Y, Sirakov BT, Epstein AH, Tan CS. Aerothermodynamics of micro-turbomachinery. In: ASME turbo expo, Vienna, Austria; 2004 [ASME Paper GT2004-53877].
- [25] Zehnder M. Efficient air–water heat pumps for high temperature lift residential heating, including oil migration aspects, PhD thesis. Ecole Polytechnique Federale de Lausanne; 2004.
- [26] SIA. Standart sia 381/3; 1982.
- [27] SIA. Standart sia 384/2; 1988.
- [28] Schiffmann J. Integrated design, optimization and experimental investigation of a direct driven turbocompressor for domestic heat pumps. PhD thesis, Ecole Polytechnique Federale de Lausanne; 2008.
- [29] Schiffmann J, Favrat D. Theoretical design of a high-speed low power radial turbocompressor. In: sixth European turbomachinery conference, Lille, France, vol. 2; 2005 [RC-057-01/71].
- [30] Cumpsty NA. Compressor aerodynamics. Malabar, FL, USA: Krieger Publishing Company; 2004.
- [31] Zangeneh M, Dawes WN, Hawthorne WR. Three dimensional flow in radial-inflow turbines. In: ASME gas turbine and aeroengine congress and exposition, Amsterdam, Netherlands; 1988 [ASME-Paper 88-GT-70].
- [32] Zangeneh M, Goto A, Harada H. On the design criteria for suppression of secondary flows in centrifugal and mixed flow impellers. *Journal of Turbomachinery* 1998;120(4):723–735.
- [33] Demeulenaere A, Hirsch C. Application of multipoint and multistage optimization to the design of turbomachinery blades. In: sixth European turbomachinery conference, Lille, France, vol. 2; 2005 [OPTI- 097-01/148].
- [34] Harinck J, Alsalihi Z, Van Buijtenen JP, Van den Braembussche RA. Optimization of a 3d radial turbine by means of an improved genetic algorithm. In: sixth European turbomachinery conference, Lille, France, vol. 2; 2005 [OPTI- 098-02/162].
- [35] Keskin A, Bestle D. Application of multi-objective optimization to axial compressor preliminary design. *Aerospace Science and Technology* 2006;10(7):581–589.
- [36] Whitfield A, Baines NC. Design of radial turbomachines. Longman Scientific; 1990.
- [37] Galvas MR. Fortran program for predicting off-design performance of centrifugal compressors. Technical Report TN D-7487. NASA; 1973.
- [38] Coppage JE, Dallenbach F, Eichenberger HP, Hlavaka GE, Knoernschild EM, Van Le N. Study of supersonic radial compressors for refrigeration and pressurization systems. Technical Report WADC TR 55-257. Air Research Manufacturing Company; 1956.

- [39] Rodgers C. Impeller stalling as influenced by diffusion limitations. *Journal of Fluids Engineering* 1977;99:84–97.
- [40] Rodgers C. A diffusion factor correlation for centrifugal impeller stalling. *Journal of Engineering for Power* 1978;100:592–603.
- [41] Daily JW, Nece RE. Chamber dimensions effects on induced flow and frictional resistance of enclosed rotating disks. *Journal of Basic Engineering* 1960;82:217–232.
- [42] Stanitz JD. One-dimensional compressible flow in vaneless diffusers of radial- and mixed-flow centrifugal compressors, including effects of friction, heat transfer and area change. Technical Report TN 2610. National Advisory Committee for Aeronautics (NACA); 1952.
- [43] Japikse D. Advanced diffusion levels in turbocharger compressors and component matching. In: IMechE conference on turbocharging and turbochargers; 1982. p. 143 [Paper C45/82].
- [44] Jansen W. Rotating stall in a radial vaneless diffuser. *Journal of Basic Engineering* 1964;86:750–758.
- [45] Senoo Y, Kinoshita Y. Influence of inlet flow conditions and geometries of centrifugal vaneless diffuser on critical flow angle for reverse flow. *Journal of Fluids Engineering* 1977;99:98–103.
- [46] Senoo Y, Kinoshita Y. Limits of rotating stall and stall in vaneless diffusers of centrifugal compressors. In: ASME Turbo Expo, London, United Kingdom; 1978 [ASME-Paper 78-GT-19].
- [47] Japikse D. Centrifugal compressor design and performance. Concepts ETI, Inc; 1996.
- [48] Lemmon E, McLinden M, Huber M. Nist reference fluid thermodynamic and transport properties. In: Standard Reference Database 23; 2002.
- [49] Leyland GB. Multi-objective optimization applied to industrial energy problems. PhD thesis, Ecole Polytechnique Federale de Lausanne; 2002.
- [50] Molyneux A. A practical evolutionary method for the multi-objective optimization of complex energy systems, including vehicle drivetrains. PhD thesis, Ecole Polytechnique Federale de Lausanne, 2002.
- [51] University of Dayton. Average daily temperature average. See, <http://www.engr.udayton.edu/weather/>; 1995–2009.